RESEARCH ARTICLE

Energy & Environmental Materials WILEY

The Perovskite Solar Cell

Unraveling the Morphological and Energetic Properties of 2PACz Self-Assembled Monolayers Fabricated With Upscaling Deposition Methods

Silvia Mariotti, Ilhem Nadia Rabehi, Congyang Zhang, Xiaomin Huo, Jiahao Zhang, Penghui Ji, Tianhao Wu, Tongtong Li, Shuai Yuan, Xiaomin Liu, Ting Guo, Chenfeng Ding, Hengyuan Wang, Annalisa Bruno, Luis K. Ono, and Yabing Qi**

Self-assembled monolayers (SAMs) are widely used as hole transport materials in inverted perovskite solar cells, offering low parasitic absorption and suitability for semitransparent and tandem solar cells. While SAMs have shown to be promising in small-area devices (≤1 cm^2), their application in larger areas has been limited by a lack of knowledge regarding alternative deposition methods beyond the common spin-coating approach. Here, we compare spin-coating and upscalable methods such as thermal evaporation and spray-coating for [2-(9H-carbazol-9-yl)ethyl]phosphonic acid (2PACz), one of the most common carbazole-based SAMs. The impact of these deposition methods on the device performance is investigated, revealing that the spray-coating technique yields higher device performance. Furthermore, our work provides guidelines for the deposition of SAM materials for the fabrication of perovskite solar modules. In addition, we provide an extensive characterization of 2PACz films focusing on thermal evaporation and spray-coating methods, which allow for thicker 2PACz deposition. It is found that the optimal 2PACz deposition conditions corresponding to the highest device performances do not always correlate with the monolayer characteristics.

1. Introduction

Perovskite solar cells (PSCs) are among the most promising next-generation photovoltaic (PV) thin film technologies due to their low-cost precursors,[1,2] energy-efficient fabrication processes,[3,4] and remarkable power conversion efficiency (PCE) up to 26.1%.[5,6] Also, PSCs with the inverted structure are gaining popularity due to their negligible hysteresis, low-temperature processing, and application in flexible and tandem solar cells.[7,8] Lately, self-assembled monolayers (SAMs) have attracted high interest by the research community for the fabrication of inverted PSCs, as they are effective in reducing non-radiative recombination losses[9] leading to an increased open circuit voltage (V_{OC}), and their ability to reduce parasitic absorption thanks to their small thickness.[10,11]

In recent years, carbazole-based organic SAMs with hole-selectivity properties, such as [2-(9H-carbazol-9-yl)ethyl]phosphonic acid (2PACz), [2-(3,6-dimethoxy-9H-carbazol-9-yl) ethyl]phosphonic acid (MeO-2PACz), and [4-(3,6-dimethyl-9H-carbazol-9-yl)butyl]phosphonic acid (Me-4PACz), originally developed by Albrecht and coworkers[10,11] gained popularity as replacement for the conventional hole transporting layers (HTLs). They all have in common a carbazole moiety that allows hole extraction and a phosphonic acid (PA) group, which ensures the formation of a covalent bond with the transparent conductive oxide (TCO) material, the starting substrate for perovskite solar cells.[12] The formation and tunability of dipole moments employing SAMs are important features that have been thoroughly investigated in the literature.[10,11,13,14] For instance, the interfacial dipole generated by SAMs between the perovskite and indium tin oxide (ITO) contributes to reducing the open circuit voltage (V_{OC}) losses in p-i-n devices owing to the better energy level alignments between SAMs and the perovskite.[10,11,13–15]

Traditionally, SAMs are deposited via spin-coating, which is the main solution-based process used in research laboratories, allowing for fast and simple depositions to achieve high device performance in small active area PSCs (e.g., from ~0.1 cm^2 up to 1 cm^2).[11] However, in the p-i-n device architecture, all the device layers have been

Dr. S. Mariotti, I. N. Rabehi, Dr. C. Zhang, X. Huo, J. Zhang, Dr. P. Ji, Dr. T. Wu, Dr. T. Li, Dr. S. Yuan, X. Liu, T. Guo, Dr. C. Ding, H. Wang, Dr. L. K. Ono, Prof. Y. Qi
Energy Materials and Surface Sciences Unit (EMSSU), Okinawa Institute of Science and Technology Graduate University (OIST), 1919-1 Tancha, Onna-son, Kunigami-gun, Okinawa 904-0495, Japan
E-mail: katsuya.ono@oist.jp
E-mail: yabing.qi@oist.jp
C. Zhang
State Key Laboratory of Organic Electronics and Information Displays & Institute of Advanced Materials (IAM), Nanjing University of Posts & Telecommunications, 9 Wenyuan Road, Nanjing 210023, China
Prof. A. Bruno
School of Physical and Mathematical Science & School of Materials Science Engineering & Energy Research Institute @ NTU Nanyang Technological University, 50 Nanyang Avenue, Singapore 639798, Singapore
The ORCID identification number(s) for the author(s) of this article can be found under https://doi.org/10.1002/eem2.12825.

DOI: 10.1002/eem2.12825

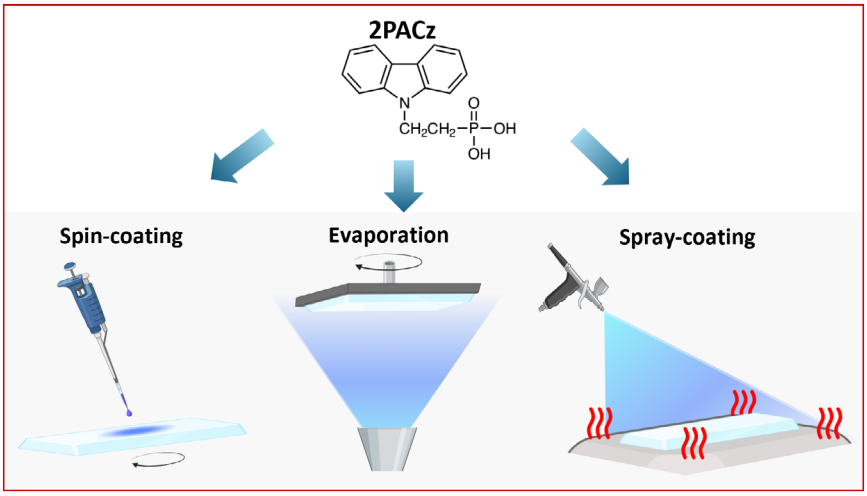

Figure 1. Schematics of the deposition and optimization methods for 2PACz using spin-coating, evaporation, and spray-coating.

demonstrated to be deposited using techniques suitable for larger areas, with the exception of SAMs. For instance, other HTLs such as nickel oxide (NiO_X) layers are deposited using techniques such as sputtering and atomic layer deposition (ALD),[16,17] while the perovskite layer is applied through upscalable methods including thermal evaporation, blade-coating, and chemical vapor deposition.[16,18,19] Additionally, fullerene (C_{60}), bathocuproine (BCP), and silver electrode layers are deposited through thermal evaporation, and tin oxide (SnO_2) and TCO layers are applied using ALD and sputtering, respectively, particularly in the case of semitransparent devices.[20]

Therefore, identifying alternative deposition methods for SAMs is essential for fabricating devices using only large-area compatible techniques. Recently, Farag et al.[21] have shown that it is possible to use a vacuum-based evaporation technique of most common SAM-HTLs including 2PACz, MeO-2PACz, and Me-4PACz. For example, PSCs based on evaporated 2PACz (with 10.5 mm^2 active area) generated a slightly higher power conversion efficiency (PCE of 18.9%) compared to that of solution-processed counterpart (18.5%). Similarly, comparable PCEs were reported when comparing the evaporated and spin-coated MeO-2PACz-based PSCs. Additionally, the wettability of the perovskite films was enhanced by employing the vacuum-deposited Me-4PACz, resulting in a corresponding PCE of around 19.3% in PSCs.[21] Thermal evaporation of these SAMs not only provides an easy technique for fabricating large area perovskite devices, but could also be used for depositing SAMs on not even surfaces, such as textures silicon surfaces in perovskite–silicon tandems applications.[22] Cassella et al.[23] employed ultrasonic spray-coated MeO-2PACz to fabricate $MAPbI_3$ PSCs, both with and without an antireflective coating, achieving PCEs of 20.3% and 18.4%, respectively, on an active area of 2.5 mm^2. These findings are fundamental for the future commercialization of large-area perovskite solar devices, as these techniques are suitable for upscaling and are widely used in industrial production lines.[24] However, none of these upscaling techniques have been used to fabricate large-area PSCs yet and a thorough characterization of the evaporated and spray-coated SAMs and their comparison are missing. 2PACz was chosen as SAM in this study because of the better hole transfer and enhanced molecular dipole as compared to MeO-2PACz[14] and the improved perovskite wettability compared to Me-4PACz.[25] Although the wettability of the perovskite on Me-4PACz improves when this is thermally evaporated,[21] our work focuses solely on 2PACz. This is because we compare vacuum and solution-processed deposition methods, and the latter would require the use of an additive for the Me-4PACz case to increase the perovskite wettability, thus making the different deposition processes not comparable.

Here, we employ thermal evaporation and spray-coating techniques for depositing 2PACz (**Figure 1**) and demonstrate how to optimize these deposition techniques. We first studied the effects of the deposition methods on small area devices, and then used the optimized conditions to fabricate proof-of-concept solar modules with an aperture area of 22.4 cm^2. We show that both evaporation and spray-coating methods are viable deposition techniques for the fabrication of PSCs and modules, after performing a thorough optimization. Similar performances are obtained from the conventional spin-coating and the optimized evaporated and spray-coating deposition methods, with slight improvements observed in the case of spray-coating. In addition, the morphology, surface potential, and light transmission of the 2PACz films prepared via spin-coating, thermal evaporation, and spray-coating are compared to identify the most effective deposition method and its effects on device performances. Evaporation and spray-coating techniques show the incredible advantage of providing control over the thickness of the deposited layer, in contrast to spin-coating. This allows for an unprecedented characterization of this material. We use X-ray photoelectron spectroscopy (XPS) to determine the thickness of 2PACz and realize that the optimized as-deposited spray-coated 2PACz thickness is above that of a monolayer. Furthermore, we find a correlation between the work function (WF) and the thickness of 2PACz. Utilizing these insights, we investigate the band alignment between 2PACz and the perovskite layer, aiming to optimize the performance for different perovskite compositions with bandgaps of 1.57 and 1.68 eV.

2. Results and Discussion

In this work, we compare three deposition methods for 2PACz, i.e., the traditional spin-coating method, as well as the upscalable thermal evaporation and spray-coating methods. We employ an inverted PSC architecture consisting of glass/indium tin oxide (ITO)/2PACz/perovskite/phenethylammonium iodide (PEAI)/phenyl-C_{61}-butyric acid methyl ester (PCBM)/bathocuproine (BCP)/Ag (Figure S1, Supporting Information). For the perovskite, a triple cation composition of $Cs_{0.05}(FA_{0.83}MA_{0.17})_{0.95}Pb(I_{0.95}Br_{0.05})_3$ with a bandgap of 1.57 eV was used for the fabrication of small area devices. Details of the deposition materials and processes are presented in the Experimental Section. Identical devices were fabricated using 2PACz either evaporated or spray-coated, for which the deposition processing required a thorough optimization. Throughout this article, we will refer to 2PACz as films or layers. Although this nomenclature is not accurate for monolayer cases, we will present 2PACz thicknesses above that of monolayers, and hence, for simplicity, we use films or layers for all 2PACz depositions.

2.1. Thermal Evaporation of 2PACz

For the optimization of 2PACz by thermal evaporation, four different thicknesses of 1, 10, 50, and 100 nm were evaluated. The deposition was performed under a vacuum of 2–3 × 10^{-4} Pa. The thickness of the evaporated 2PACz layer was measured using a quartz crystal microbalance (QCM), which was calibrated a priori by comparing the thickness shown in QCM with the actual thickness measured by atomic force microscopy (AFM). The performances of PSCs were assessed in relation to the thickness of the evaporated 2PACz (Figure S2 and Table S1, Supporting Information). The as-deposited thicker 2PACz films showed an increased V_{OC} (1.16 and 1.08 V on average at thicknesses of 50 and 100 nm, respectively) and short-circuit current density (J_{SC}) (21.3 mA cm^{-2} on average for both 50 and 100 nm thicknesses). PSCs with evaporated 2PACz layers achieved an average PCE of 17.2% and 15.8% with 50 and 100 nm 2PACz thicknesses, respectively. These values are significantly lower than the 19.7% average PCE achieved with spin-coated 2PACz (Figure S3 and Table S1, Supporting Information).

To further enhance the PCE of the evaporated 2PACz, we performed a postdeposition treatment that consists of annealing at 100 °C for 5 min after evaporation, followed by washing (with ethanol through spin-coating at 3000 rpm for 15 s), and a second annealing step (100 °C for 5 min) to evaporate the remaining solvent. Farag et al. have reported a different postdeposition treatment method, which involves dripping ethanol ~5 s before the spinning is started followed by dynamic dripping of ethanol every 10 s during a total of 40 s of spin-coating process.[21] After implementing our postdeposition treatment method, we noticed that the devices using thinner 2PACz (1 and 10 nm) exhibited PCEs similar to those of nontreated devices. In contrast, the devices incorporating thicker 2PACz layers with postdeposition treatment (50 and 100 nm) showed improved performance, as evidenced by average PCEs of 7.9%, 13.3%, 19.3%, and 17.0% for 1, 10, 50, and 100 nm, respectively (**Figure 2a**).

Trends in device parameters such as V_{OC}, J_{SC}, and fill factor (FF) are presented in Figure S2 and Table S1, Supporting Information. The highest device performances are achieved using 50–nm-thick 2PACz with the postdeposition treatment. For comparison, the average PCEs of devices with 50–nm-thick 2PACz without and with postdeposition treatment are 17.2% and 19.3%, respectively. The FF has increased from 70.0% to 79.8% leading to major contribution in PCE, as shown in Figure S2, Supporting Information. We notice that the postdeposition treatment is advantageous for thicker layers (evaporated 50 and 100 nm evaporated 2PACz) only. This suggests that the extremely thick 2PACz layers negatively affect the device performance. On the other hand, the postdeposition treatment addresses this issue by removing the excess 2PACz, especially the molecules that have no covalent bonding with the ITO, resulting in thinner 2PACz layers. However, regardless of the postdeposition treatment, by increasing the thickness of the evaporated 2PACz, the probability of surface coverage (with covalent bonding between the 2PACz and ITO) is increased. Hence, this suggests that the ethanol washing selectively removes the excess 2PACz, leaving the covalently bonded 2PACz intact. Additionally, the packing of 2PACz molecules on the ITO surface is enhanced with increasing 2PACz thicknesses evaporated on the substrates. A schematic of this proposed mechanism is presented in Figure 2b, and more details are provided in the subsequent sections.

2.2. Spray-Coating of 2PACz

Regarding the spray-coating deposition, a solution of 2PACz (1 mg mL^{-1}) in ethanol was spray-coated onto glass/ITO substrates placed on a hotplate at 100 °C. The airbrush was maintained at a distance of about 15 cm from the substrate during the process. The optimization has been done using different cycles, namely 1, 5, 10, and 20 cycles (Figure 2c). One airbrush spray pass (left-to-right) is counted as one cycle (abbreviated as "cy"). Because it was challenging to measure the actual layer thickness by AFM due to the rather large local roughness of the spin-coated films, we used the Tougaard noninteractive method to estimate the thickness,[26] which was determined to be 2.2, 5.3, 7.1, and 8.4 nm for 1, 5, 10, and 20 cycles, respectively (Figure S4, Note S1, Supporting Information). The morphology of 2PACz films is discussed in Section 2.4. in more detail. Figure 2d shows a representative *J-V* curve of a device with 10 cycles spray-coated 2PACz being the optimized condition for this deposition method with a PCE of 20.59%, V_{OC} = 1.17 V, J_{SC} = 22.52 mA cm^{-2}, and FF = 78.4% (with all the device parameters shown in Figure S5 and Table S2, Supporting Information, with averages being PCE = 20.0%, V_{OC} = 1.15 V, J_{SC} = 22.4 mA cm^{-2}, and FF = 77.5%). To have a direct comparison with the evaporated 2PACz, postdeposition treatments were conducted on 1, 5, 10, and 20 cycles spray-coated 2PACz (Figure 2c and Figure S5, Supporting Information). However, for the spray-coated 2PACz PSCs, the PCE drops considerably after the postdeposition treatment, mainly due to the reduced V_{OC}. For example, considering the optimized condition of 10 cycles, the average PCE goes from 20.0% to 14.7% after the postdeposition treatment, and the average V_{OC} goes from 1.15 to 0.96 V (Figure S5, Supporting Information). Therefore, we did not adopt the postdeposition treatment for the spray-coated 2PACz.

When comparing PSCs fabricated with evaporated and spray-coated 2PACz, a consistent trend is observed in devices without the postdeposition treatment. Specifically, an increase in 2PACz thickness correlates with better coverage on ITO enhancing V_{OC} and J_{SC}. This is attributed to the surface passivation and interface dipole formation by 2PACz,[10] thereby contributing to the observed enhancements in V_{OC} and J_{SC}. Indeed, it is widely acknowledged that a full coverage not only increases V_{OC} but also improves the FF.[27] However, while devices with evaporated 2PACz show an increased FF with the thickness, this decreases in the case of spray-coated devices. We believe that increasing the thickness could limit the FF due to the poor conductivity of 2PACz, affecting the series resistances of devices (Figure S6, Supporting Information). Disentangling the effects that affect all parameters can be challenging, mainly due to the different experimental factors used for the two techniques, which may influence the final device performance. Examples of the experimental factors are the deposition process (vacuum conditions and high processing temperature for the evaporated 2PACz) and the UV-O_3 treatment. In fact, substrates were immediately transferred from the UV-O_3 cleaner onto the hotplate for the spray-coating of 2PACz with a short air exposure time. On the other hand, a longer air exposure time was unavoidable for the UV-O_3 treated ITO due to the substrate positioning onto the masks for the evaporation and the starting of the vacuum pump. In addition, the long vacuum exposure time of the UV-O_3-treated ITO substrates before the thermal evaporation of 2PACz could affect the surface activation of ITO. These factors may strongly affect the packing system of 2PACz,[28] and consequently, the device performance.

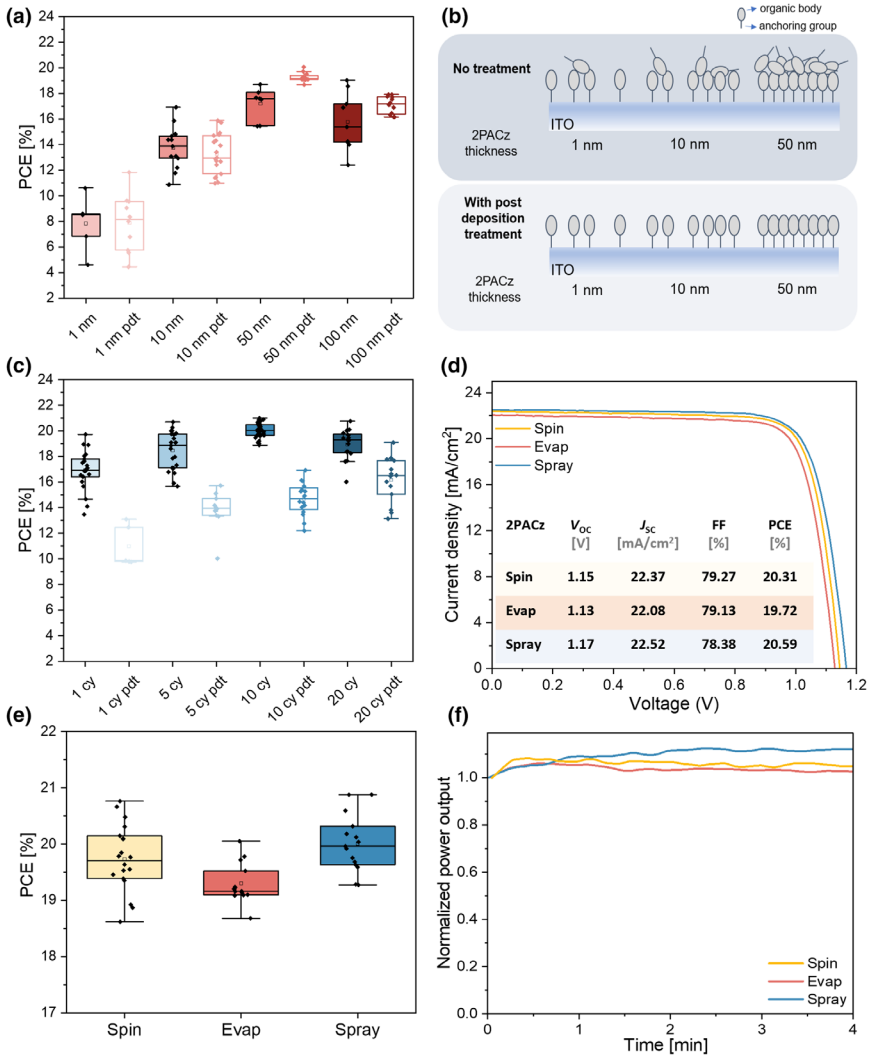

Figure 2. a) Device performances of 1, 10, 50, and 100 nm evaporated 2PACz without and with postdeposition treatment (abbreviated as pdt). b) Schematic illustration of a proposed mechanism of increasing the evaporated 2PACz thickness, with and without postdeposition treatment. c) Device performances of 1, 5, 10, and 20 cycles (cy) 2PACz deposited via spray-coating. d) *J-V* curves with inset presenting the solar cell parameters, e) box charts showing the performance comparisons, and f) the MPP tracking (4 min) of representative devices with 2PACz deposited by the optimized spin-coating, thermal evaporation, and spray-coating methods. The power output values are normalized at 0 min.

As discussed in detail later, the washing treatment produces monolayers (**Figure 2**b). For the evaporated 2PACz devices, the postdeposition treatment shows an increment of the FF, with particular benefit in thicknesses of 50 and 100 nm (Figure S2, Supporting Information). In particular, in the case of devices with 50 nm evaporated 2PACz, the FF increases from 70% to 79.8% after the postdeposition treatment. This correlates to the higher series resistance observed in devices without the postdeposition treatment, particularly in thicker films (39.0 and 22.4 Ω cm^2) without and with postdeposition treatment, respectively (Figure S6, Supporting Information). As for devices with spray-coated 2PACz, the postdeposition treatment slightly increases the FF, but causes a significant decrease of V_{OC} and J_{SC}, causing the PCE to drop (Figure S5, Supporting Information). Thus, for higher device performances of evaporated 2PACz PSCs, the postdeposition treatment is essential, while for spray-coated 2PACz devices, the postdeposition treatment is not necessary. To compare the device performances of our 2PACz-based small devices, we performed a literature survey analyzing the J_{SC} and FF values of perovskite devices with similar composition (mostly triple cation) and band gap (from 1.55 to 1.6 eV) fabricated using not only 2PACz, but also including other type of SAMs (MeO-2PACz, Me-4PACz, (7-(4-(diphenylamino)phenyl) benzo[c][1,2,5]thiadiazol-4-yl)phosp-hornic acid (PPA), benzo[rst]pentaphene (SA-BPP), (2-(4-(bis(4-methoxyphenyl)amino)phenyl)-1-cyano vinyl)phosphonic acid (MPA-CPA), and so on) as well as other traditional HTLs including poly(bis(4-phenyl)(2,4,6-trimethylphenyl)amine) (PTAA), 2,2′,7,7′-Tetrakis[N,N-di(4-methoxyphenyl)amino]-9,9′-spirobifluorene (spiro-OMeTAD), and NiO_X (Figure S7, Supporting Information).[23,29–44] We notice that different strategies are adopted to increase the J_{SC}, for example, using antireflection coatings,[29,36,41,44] and adopting different methods to increase the crystalline size from 500 nm up to 1 um[23,37,40,44] resulting in enhancement of both J_{SC} and FF. Nevertheless, comparing the reported J_{SC} and FF considering only the 2PACz-based devices, our devices are within the values of reported references.[28,36,40,43] Additional SEM measurements performed on our perovskite devices (cross section, Figure S8a, Supporting Information) show that the perovskite thickness is about 550 nm, being a reasonable thickness for achieving good device performances. SEM top view (Figure S8b, Supporting Information) shows a dense and compact perovskite film but with grain size ranging from small (175 nm) to larger grains (570 nm), while an increased size uniformity and larger grains are expected to further increase the J_{SC}.

After finding the optimum conditions for the evaporated and spray-coated 2PACz, we compared them to the conventional spin-coating method. Figure 2d shows representative *J-V* curves and Figure 2e shows the PCEs of solar cells using different deposition methods of 2PACz (average PCE of 19.7%, 19.3%, and 20.0% for spin-coated, evaporated, and spray-coated 2PACz PSCs, respectively). The corresponding maximum power point tracking (MPPT) and box charts revealing the average device parameters are shown in Figure 2f and Figure S3, Supporting Information, respectively. The performances of devices do not have significant differences, and hence, both evaporation and spray-coating techniques are considered valid deposition techniques for the fabrication of small area solar cell devices, as also confirmed by Farag et al.[21] and Cassella et al.[23]

In addition, our results show that spin-coated, evaporated, and spray-coated 2PACz show low hysteresis (Figure S9a–c, Supporting

Information). The external quantum efficiency (EQE) measurement shows similar results between the optimized PSCs. The integrated J_{SC} values, derived from EQE (Figure S9d–f, Supporting Information) for spin-coated, evaporated, and spray-coated 2PACz-based PSCs are 22.52, 22.4, and 22.48 mA cm^{-2}, respectively. These values align closely with the J_{SC} values obtained from the *J-V* curves (Figure 2d). In addition, the bandgap measured from EQE shows a consistent value of ~1.57 eV for all the devices (Figure S9, Supporting Information). The long-term stability assessments conducted with unencapsulated devices under N_2 flow at 29 °C–30 °C show a PCE drop of around 0.04%, 0.27%, and 0.04% for spin-coated, evaporated, and spray-coated 2PACz devices, respectively, after 150 h of continuous illumination and steady-state power output (SPO) (Figure S9g–i, Supporting Information). Spray-coated 2PACz devices have been measured also up to 1000 h showing stable SPO (>T_{80}) (Figure S10, Supporting Information). These results reveal that spin- and spray-coated 2PACz confer greater stability compared to evaporated 2PACz devices.

The differences in the device stability (Figure S9g–i, Supporting Information) might be related to the quality of 2PACz films. To verify this hypothesis, we compare the powders of fresh 2PACz, and the material left on the crucible after the thermal deposition. First, a visual inspection shows color differences, with the fresh whitish 2PACz powder turning into a gray-colored powder after the thermal evaporation (Figure S11a, Supporting Information). By adding a thermocouple in the crucible together with the fresh 2PACz powder, we observed a temperature increase from 20 °C to 150 °C when the evaporation rate starts (0.1–0.5 Å s^{-1}). The temperature further increased up to 234 °C when reaching a thickness of 50 nm, at a rate of 0.22 Å s^{-1} (Figure S11b, Supporting Information). This condition surpasses the melting temperature of 2PACz (231 °C), as specified by the manufacturing company.[45] Thus, we performed thermal gravimetric analysis (TGA) coupled with differential thermal analysis (DTA) to determine mass changes in the powder as a function of temperature and the temperature difference between the sample and a stable reference material (Al_2O_3), respectively. As shown in Figure S11c, Supporting Information, we observed that for TGA, the mass loss starts at 217 °C and that the DTA spectra show two peaks in the same region, which correspond to release of heat, one at 217 °C and another at 231 °C, the latter being in agreement with the temperature reported for the melting point of 2PACz. Thus, the degradation of the 2PACz may occur before the melting point (217 °C). To confirm this, we analyzed the powders of fresh 2PACz, and the material left on the crucible after thermal deposition and found by attenuated total reflectance (ATR) analysis that the two powders show significant differences (Figure S11d,e, Supporting Information). Most changes appear at lower wavenumbers (1750–400 cm^{-1}), corresponding to C-N stretching, and C=C and C–H bending. Therefore, the temperature of the crucible at a low rate (0.5 Å s^{-1}, 150 °C) for very thin thicknesses (1–5 nm) can preserve the molecular properties. On the other hand, when using the optimized recipe of 50-nm-thick evaporated 2PACz with postdeposition treatment, the properties of the 2PACz molecules are not preserved, leading to poor long-term stability (Figure S9g–i, Supporting Information). However, it should be noted that by controlling the crucible temperature of 2PACz and maintaining a low evaporation rate, the chemical properties may be preserved.

In the following paragraphs, we will analyze the morphological and energetic properties of the 2PACz layers deposited using the three deposition methods, and the characteristics of the perovskite layer grown on top.

2.3. Perovskite Films on 2PACz by Spin-Coating, Evaporated, and Spray-Coating

The wettability of the perovskite precursor solution on spin-coated, evaporated, and spray-coated 2PACz films has been checked through contact angle measurements, revealing no major differences (Figure S12, Supporting Information). Spin-coated, evaporated, and spray-coated 2PACz show low contact angles of ~ 10°, 17°, and 12°, respectively, indicating that all 2PACz layers have good wettability properties with the perovskite precursor solution. The perovskite surface morphology was characterized using scanning electron microscopy (SEM). The perovskite films deposited on spin-coated, evaporated, and spray-coated 2PACz films, were not affected by the deposition methods of 2PACz (Figure S13, Supporting Information). Photoluminescence (PL) spectra of the perovskite films deposited on the 2PACz layers are shown in Figure S14, Supporting Information. The spectra include perovskite on evaporated 2PACz with different thicknesses, both with and without postdeposition treatment (Figure S14a,b, Supporting Information), spray-coated with different cycles (Figure S14c, Supporting Information), and the comparison of all optimized methods (Figure S14d, Supporting Information). The general behavior is described by increased PL intensity for increased 2PACz thickness (for both evaporated and spray-coated layers). In fact, for monolayer thickness of 2PACz, PL of perovskite usually increases as non-radiative recombination losses decrease. On the other hand, in the case of thick 2PACz layers, the PL intensity increases because charge transfer between perovskite and ITO is suppressed by the insulating properties of the carbazole-based SAMs.[46] One exception is found for the evaporated 2PACz layer, which at 100 nm thickness shows a reduced PL intensity. The same trend is shown for evaporated 2PACz layers with the postdeposition treatment, where the PL reduction is more significant. The thick 100 nm layer obtained using elevated evaporation rates demonstrated changes in the properties of 2PACz (Figure S11, Supporting Information). These modifications can further influence the interaction with the perovskite, and consequently affect the PL results. The spray-coated 2PACz shows higher PL intensity compared to the spin-coated and evaporated 2PACz, which suggests reduced non-radiative recombination losses.[47] These results agree with the device performance trends, where the highest V_{OC} average of 1.16 V was achieved in devices with spray-coated 2PACz, compared to spin-coated (V_{OC} = 1.14 V) and evaporated (V_{OC} = 1.11 V) 2PACz.

2.4. Morphology and Energetic Properties of 2PACz

The morphology of the 2PACz layers deposited via spin-coating and optimized evaporation and spray-coating methods were explored by AFM (**Figure 3**a–c). The spin-coated 2PACz shows a root mean square (RMS) roughness of 2.48 nm, being similar to that of ITO (2.46 nm). Spin-coated SAM HTLs are well known for covering conformally rough surfaces within a self-limiting process.[10,11] In the case of evaporated 2PACz films, the RMS values of the 50 nm evaporated 2PACz are 2.90 and 2.93 nm before and after the postdeposition treatment, respectively, showing a negligible increase of RMS (Figure S15, Supporting Information). For the spray-coated films, the RMS decreases with increasing the number of cycles (3.25, 3.12, 3.02, and 2.95 nm for 1, 5, 10, and 20 cycles, respectively, Figure S16, Supporting Information). The RMS values for spin-coated and evaporated 2PACz are in agreement with the SEM images (Figure S17a, Supporting

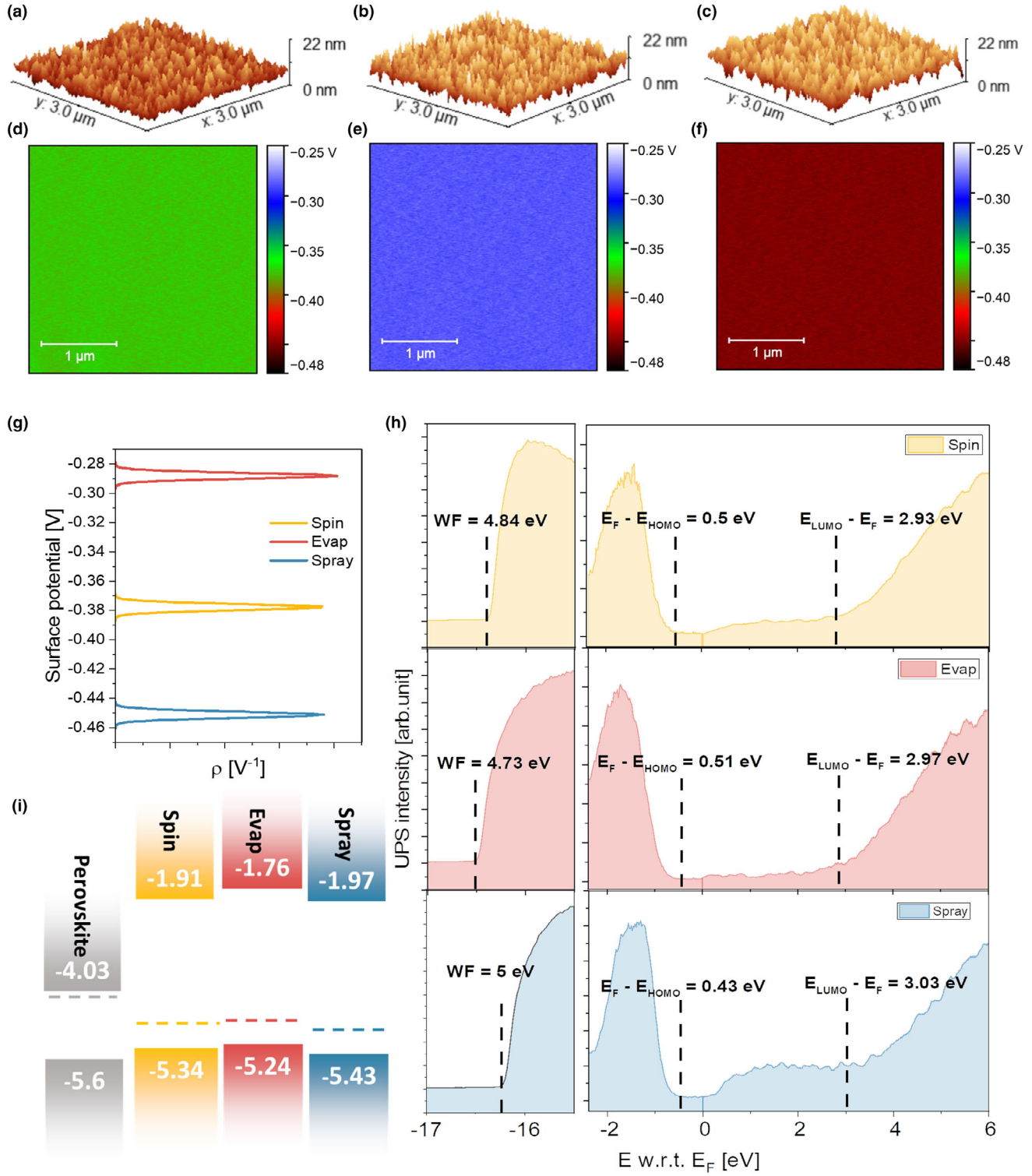

Figure 3. a–c) Simultaneous AFM and d–f) KPFM measurements for extracting the root-mean-square (RMS) surface roughness and contact potential difference (CPD) values of optimized 2PACz layers deposited by spin-coating a, d), evaporation b, e), and spray-coating c, f). g) KPFM CPD distribution (ρ) profiles showing surface potential of −0.38, −0.29 and −0.45 V of 2PACz layers (high CPD values correspond to high WF values), deposited via spin-coating, evaporation, and spray-coating respectively. h) Combined UPS and low-energy inverse photoemission spectroscopy (LEIPS) spectra of spin-coated, evaporated, and spray-coated 2PACz films showing the differences in the HOMO and LUMO levels (energy with respect to Fermi level). i) Energy level alignments between the perovskite film (triple cation) and spin-coated, evaporated, and spray-coated 2PACz, showing their HOMO, LUMO, and WF.

Information), where smooth films are formed, and no feature can be observed on their surface. However, this changes in the case of the spray-coated 2PACz SEM images (Figure S17b, Supporting Information). The 1, 5, 10, and 20 cycles 2PACz films show rough surfaces for all cycles and even at the highest magnification (scale bars correspond to 20 μm), with round-shaped features that resemble the shape of bubbles caused by droplets drying quickly, as the deposition is performed on a hot plate.

To gain further insights into whether the perovskite solution during its deposition could alter the 2PACz morphology, N,N-dimethylformamide (DMF) solvent (without the perovskite precursor) was spin-coated on the spray-coated 2PACz film. The SEM images revealed a smooth morphology without the bubbles, corroborating with the fact that 2PACz film morphology is prone to changes during the perovskite precursor solution deposition (Figure S18, Supporting Information). Because the SEM magnification is lower than that of AFM (3×3 μm^2), we believe that the RMS measured by AFM are reliable only on the considered small areas and are not representative of the full active area of devices. According to the SEM images, the roughness of the film increases with increasing the number of cycles. In addition, we performed Kelvin probe force microscopy (KPFM) to visualize the surface potential mapping of the 2PACz films. Figure 3d–g show the contact potential difference (CPD) distributions and a similar surface potential uniformity is inferred for the 2PACz deposited by spin-coating, evaporation, and spray-coating methods. The average CPD values of −0.38, −0.29, and −0.45 V were extracted for spin-coated, evaporated, and spray-coated 2PACz layers, respectively. Several factors contribute to the CPD values such as monolayer interface dipole, WF variations in thick 2PACz films, and the eventual presence of surface charges.[15,48,49] Our KPFM results correlate with the V_{OC} trends observed in Figure S3, Supporting Information, where higher CPD values lead to enhanced V_{OC} and PCE observed for the spray-deposited 2PACz-based PSCs.

To further verify this observation, ultraviolet photoemission spectroscopy (UPS) was performed. The WF values of spray-coated 2PACz are 4.62, 4.98, 5.01, and 5.02 eV for 1, 5, 10, and 20 cycles, respectively (Figures S19 and S21, Supporting Information), which justifies the V_{OC} average values increase from 1.03, 1.08, and 1.15, to 1.14 V, respectively (Figure S5, Supporting Information). As for the evaporated 2PACz without postdeposition treatment, the WF values show a nonlinear behavior with the values of 4.73, 5.14, 4.74, and 4.72 eV for 1, 10, 50, and 100 nm, respectively (Figure S20a,b, Supporting Information). The nonlinear trend is caused by the degradation of the 2PACz when the evaporation rate reaches high values (Figure S11b, Supporting Information). Below 10 nm, the temperature of the crucible is below 200 °C, while for 50 and 100 nm the temperature reaches >200 °C leading to the degradation of 2PACz molecules. The subsequent postdeposition treatment on thick layers of evaporated 2PACz results in a constant WF values of ~4.7 eV (Figures S20c,d and S21e,g, Supporting Information), which correlates with the fact that the postdeposition treatment results in thinner layers of 2PACz (Figures S2 and S20c,d, Supporting Information). Modifications of the ITO WF induced by SAMs have been previously explained by the interfacial dipole formations employing photoemission and KPFM techniques.[10,11,13–15,50] In our studies, we aimed at investigating whether the differences in the formation of interfacial dipoles (ITO/2PACz) and their strengths could be distinguished when employing our three deposition techniques. The identification of interfacial dipoles are performed by plotting the energy levels with the Fermi level alignment ($E_F = 0$, Figure S21g,h, Supporting Information). The WF values for thin 2PACz layers show higher values than the ITO WF (4.42 ± 0.10 eV), indicating the presence of an interface dipole at the monolayer 2PACz interface with ITO.[10,11,13,15] Interestingly, the monolayer 2PACz shows a similar interface dipole strength (indicated by Δ in Figure S21g,h, Supporting Information) for the three deposition methods considering the UPS uncertainty (150 meV).[50] For example, Δ values of 0.42, 0.33, and 0.20 eV were extracted for the spin-coated, evaporated with the postdeposition treatment, and spray-coated 2PACz (one cycle), respectively (Figure 3i and Figure S21g,h, Supporting Information). The above results show the intrinsic strong bonding nature of monolayer 2PACz to ITO (i.e., the phosphonic anchoring group on ITO), which determines the interface dipole strength and is independent of the deposition techniques employed. Figure 3h,i show the WF and the highest occupied molecular orbital (HOMO) and the lowest unoccupied molecular orbital (LUMO) features of optimized spin-coated, evaporated, and spray-coated 2PACz with WF values of 4.84, 4.73, and 5 eV, respectively. These results are in agreement with the results obtained from KPFM (Figure 3d–g).[51]

The spin-coated, evaporated, and spray-coated 2PACz layers transmittance has been measured using UV–visible spectrometer (UV–Vis). As expected, the transmittance (T%) decreases when the thickness increases, for both evaporated and spray-coated 2PACz (Figure S22a,c, Supporting Information). However, after applying the postdeposition treatment for the evaporated 2PACz film, the transmittance of layers with different thicknesses becomes similar (Figure S22b, Supporting Information), which suggests that the excess 2PACz has been removed, becoming a monolayer, similar to the spin-coated 2PACz. In fact, Figure S22d, Supporting Information, shows identical transmission curves of spin-coated and 50 nm evaporated 2PACz with postdeposition treatment, while the 10 cycles spray-coated 2PACz shows a lower transmission suggesting that the spray-coated 2PACz layer is thicker.

The surface chemistry of spin-coated, evaporated, and spray-coated 2PACz films were investigated by XPS analyzing the O 1*s*, C 1*s*, N 1*s*, P 2*p*, and In 3*d* core levels (**Figure 4**a, Figures S23–S28, Tables S3 and S4, and Note S2, Supporting Information). The peak fittings and analyses were conducted with Casa XPS software.[52] The C 1*s* core-level region corresponding to monolayer thick 2PACz was previously described including three peak components of carbon bonds (C–C/C–H, C–N/C=N, and C–P at ~283.8, ~284.7, and ~285.7 eV, respectively) from 2PACz molecules and three peaks from the adventitious hydrocarbons on ITO (C–C/C–H, C–O, and C=O at ~284.7, ~286.4, and ~288.6 eV)[10,14,15] (Figure S23 and Note S2, Supporting Information). However, the lack of O 1*s* fitting model prevails in the literature due to the low signal intensity originated from the monolayer 2PACz[10] (Figure 4b). In our studies, we take the advantage of thicker 2PACz (i.e., >10 nm evaporated 2PACz) to identify the XPS peaks in the O 1*s* core-level region corresponding to the 2PACz molecules. First, we adopt the strategy reported by Al-Ashouri et al.[10] by first considering the O 1*s* components from the bare ITO substrate. In our case, four Gaussian–Lorentzian peak components (represented by black dashed lines in Figure 4a and Figure S26, Supporting Information) are observed to reproduce well the O 1*s* region of the bare ITO. The four peaks were previously assigned to (O_I) oxygen in In_2O_3/SnO_2 of ITO, (O_{II}) metal hydroxide species, (O_{III} and O_{IV}) hydroxides and adventitious contaminants at ~530.3, ~531.5, ~532.3, and ~533.4 eV, respectively.[10] Because all the 2PACz film preparations were performed in the same batch, the relative distances, and the intensity ratios of those four components were kept fixed, by using the constraint

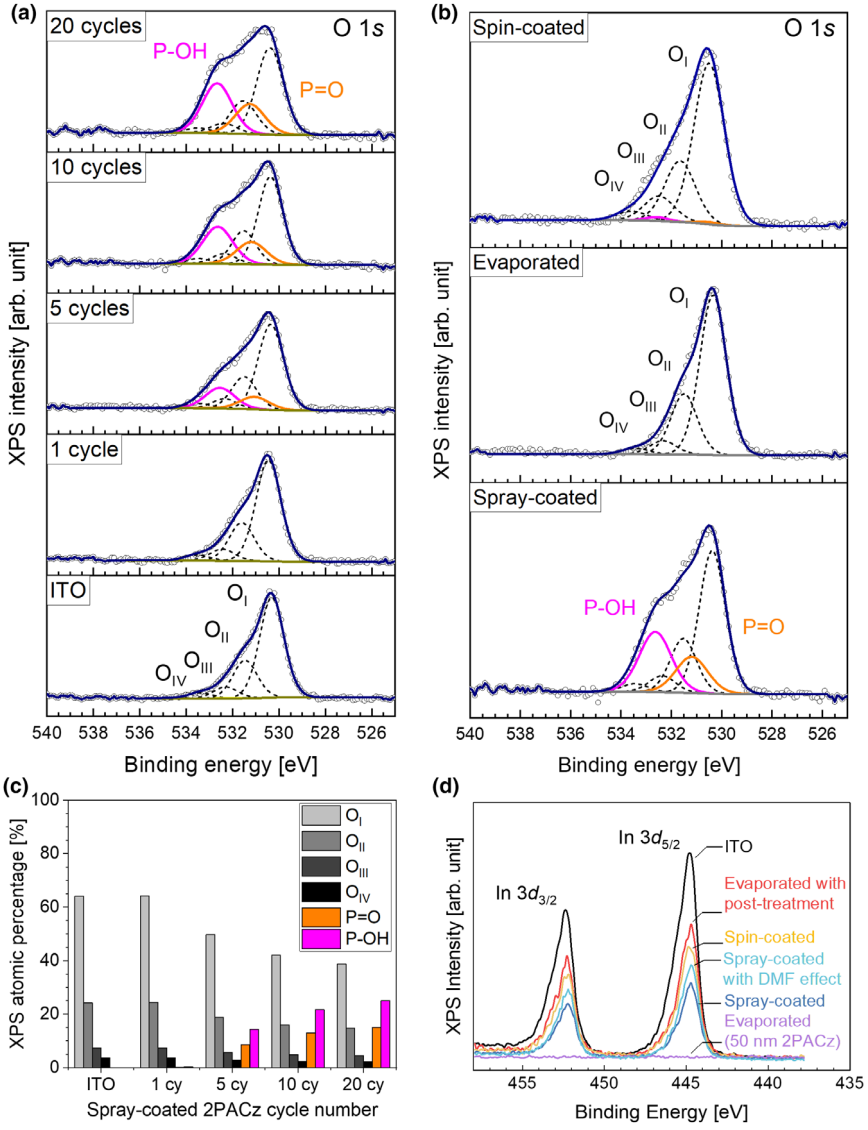

Figure 4. XPS O 1*s* core-level regions of a) spray-coated 2PACz (1, 5, 10, and 20 cycles) and the bare ITO substrate as reference and b) the optimized conditions for spin-coated, evaporated, and spray-coated 2PACz that led to the highest PCEs. c) Summary of XPS atomic percentages for the oxygen-related components in ITO (O_I, O_{II}, O_{III}, and O_{IV}) and 2PACz molecules (P=O and P–OH). d) XPS In 3*d* intensities using the three different deposition methods optimized for the highest device performances (spin-coated, 50 nm evaporated 2PACz with postdeposition treatment, and 10 cycles for spray-coated 2PACz before and after the DMF effect).

function in Casa XPS. To determine the O 1*s* XPS peak positions of 2PACz, two additional components were included in the fitting model, considering the molecular structure of 2PACz, and counting the oxygen environment within the molecule (Figure 1). Based on this methodology, we can identify the binding energy positions of P–OH and P=O bonds at 532.52 ± 0.16 eV and 531.13 ± 0.12 eV, respectively. These values are consistent with previous reports on similar SAM molecules with functional phosphonic anchoring groups.[53] The intensity ratio of [P=O]: [P–OH] ~0.6 was extracted from all the fittings, which is slightly higher than the nominal value of [P=O]: [P–OH] ~0.5 expected considering the 2PACz molecular structure (Figure 1). The observed deviation is within the XPS uncertainty estimates for atomic ratio analyses considering the several empirical factors during the photoemission processes, which are modeled using synthetic background and peak shapes.[54] When the number of cycles is increased in spray-coated 2PACz, the gradual increase in P-OH and P=O is inferred (Figure 4a,c). Similar trend is observed for the evaporated 2PACz results (Figure S26, Supporting Information), where the deposition of 10 nm leads to the appearance of P–OH and P=O peaks. Further increase in thickness (50 and 100 nm) leads to a complete attenuation of ITO related XPS peaks. Only for the one cycle spray-coated and 1 nm evaporated 2PACz, the sensitivity of 2PACz is below the detection of the XPS system, which indicates the monolayer thickness.[10] Figure 4b summarizes the XPS O 1*s* regions corresponding to the optimized conditions for spin-coated, evaporated, and spray-coated 2PACz that lead to the highest device performances (Figure 2d,e). Interestingly, the slightly higher PCEs obtained for the optimized spray-coated 2PACz correlates with the excess of 2PACz as having beneficial effects.

As mentioned before, the determination of 2PACz film thickness deposited on non-flat ITO surfaces (roughness of ~2.5 nm) was challenging. The analyses of In 3*d* peak intensities (coming from ITO in the form of In_2O_3) gives insight about the coverage of 2PACz on ITO, and hence, the thickness of the 2PACz layer (Figure 4d). Doublet peaks associated with the spin–orbit coupling are observed in the In 3*d* core levels with the intensity ratios of $[d_{5/2}]$: $[d_{3/2}]$ ~1.5. In the case of 50 and 100 nm evaporated 2PACz without postdeposition treatment, In 3*d* peaks are not observed, because of the thick 2PACz layer covering ITO attenuates the In 3*d* signal (Figure S27a, Supporting Information). Based on the universal curve for the inelastic-mean-free-path of electrons in a solid material, the probing depth in XPS does not exceed 10 nm in general.[55,56] However, after the postdeposition treatment, In 3*d* peaks show similar intensities independent of the initial 2PACz deposition thickness, inferring that the postdeposition treatment leads to reduced and similar final thicknesses (Figure S27b, Supporting Information). In addition, the evaporated 50 nm 2PACz after the postdeposition treatment shows the In 3*d* peak intensities slightly higher than that of spin-coated 2PACz (Figure 4d and Figure S27, Supporting Information), suggesting a slightly thinner 2PACz layer. The above results correlate well with the UPS results, where the similar WF values observed in UPS after the postdeposition treatment (Figures S20 and S21, Supporting Information) is explained by the resulting similar 2PACz film thicknesses (Figure S27, Supporting Information).

The 2PACz layer thickness can be estimated by the exponential decrease in XPS peak intensity based on Lambert–Beer's law (please see Ref.[15,57] for more details). Based on this reported methodology,

the thickness of 50 nm evaporated 2PACz films after the postdeposition treatment can be estimated as around 0.83 nm. This thickness is slightly lower than the spin-coated 2PACz thickness, which is estimated to be around 1.2 nm (Figure 4d and Figure S27, Supporting Information), which is close to the reported value of 1.1 nm of the 2PACz solution prepared using 1 mg mL^{-1} (3 mmol) of 2PACz in ethanol.[15] As for the optimized 10 cycles spray-coated 2PACz, the estimated thickness is 7 ~ 9 nm (Figure S28, Supporting Information), which represents the average value from the XPS detection area (700 × 300 μm^2). As previously discussed, the sprayed-coated 2PACz film morphology (SEM, Figure S17, Supporting Information) shows large features of ~50 μm in diameter, and the height measured at the edges of these features can be as high as 25 nm (AFM, Figure S29, Supporting Information). Thus, the thickness of 7–9 nm determined by XPS seems to provide a reasonable averaged value. In addition, the intensity of In 3*d* peaks show that the optimized 10 cycles spray-coated 2PACz intensity (Figure S28, Supporting Information) is lower than that of spin-coated and higher than that of 10 nm evaporated 2PACz samples (Figure S27a, Supporting Information), suggesting that the average thickness of spray-coated 2PACz with 10 cycles is around 10 nm. These estimations are in agreement with the Tougaard noninteractive method calculations previously presented in Figure S4, Supporting Information, (7.1 nm for 10 cycles spray-coated 2PACz).

As demonstrated in the SEM images in Figure S18, Supporting Information, spin-coating of DMF on the spray-coated 2PACz to simulate the effect of perovskite precursor solution spin-coating, alters the morphology of the 2PACz leading to a more uniform film on which the large features are not detectable anymore by SEM. Therefore, the thickness of the spray-coated 2PACz after the perovskite solution spin-coating is expected to change. We have performed XPS (C 1*s*, N 1*s*, O 1*s*, and P 2*p*) and UPS (Figure S30a–e, Supporting Information), to determine the thickness and work function of the spray-coated 2PACz after spin-coating DMF, called "DMF effect." Indeed, the In 3*d* peaks of the spray-coated 2PACz with DMF effect, show an increment in intensity as compared to the spray-coated 2PACz, corresponding to a thinner film (Figure 4d), despite remaining thicker than the spin-coated one. Furthermore, UPS results of 10 cycles of spray-coated 2PACz after DMF spin-coating (Figure S30e, Supporting Information) show a decrease in WF from 5.01 to 4.95 eV indicating that the thickness after DMF spin-coating is reduced, which corroborates with the XPS results. Similar to the DMF effect on the spray-coated devices, the same effect is expected to occur on thick as-deposited evaporated 2PACz films. As shown in Figure 2a, the PCE of devices without postdeposition treatment show lower performances compared to those with pdt or spin-coated 2PACz. However, they still deliver reasonable performances (PCE up to 17.2%, in the case of 50 nm 2PACz), which would not be possible with such thick films, due to the insulating properties of 2PACz molecule. Therefore, we have performed XPS analysis of the optimized condition for the evaporated devices without pdt (50 nm) before and after washing with DMF. The results presented in Figure S31a, Supporting Information, show that the as-deposited 50-nm-thick layer reaches a final thickness of ~4.2 nm after "DMF effect," measured from the C 1*s* XPS spectra using the Tougaard noninteractive method (Note S1, Supporting Information). Furthermore, Figure S31b, Supporting Information, shows the In 3*d* peaks, which are used to demonstrate how much the DMF washing affects the 2PACz thickness: before "DMF effect" the In 3*d* peaks from ITO cannot be detected, while after the "DMF effect" an intense peak appears, demonstrating that final 2PACz thickness has become considerably thinner. Despite DMF removes most of the 2PACz excess, ethanol washing (pdt) is more efficient, resulting in a thickness of 0.83 nm (Figure 4d) and higher device performances (Figure 2a).

Secondary ion mass spectroscopy (SIMS) was performed on spin-coated 2PACz/perovskite and spray-coated 2PACz/perovskite samples to investigate the possible excess of 2PACz remaining in the perovskite film (Figure S32a,b, Supporting Information). We find that the 2D SIMS measurements of spray-coated 2PACz/perovskite presents a lag in the peak appearance at m/q = 63 amu corresponding to PO_2^- signal (originating from the phosphonic acid of 2PACz), when compared to the peak appearance of m/q = 79, 81 amu (Br^-) and 127, 128 amu (I^-, HI^-) originated from the perovskite layer.[58,59] The same peak is not detected for the spin-coated 2PACz/perovskite samples, most likely due to the sensitivity limits of SIMS on the monolayer 2PACz. These results indicate the coexistence of 2PACz at the bottom and within the perovskite layer when using spray-coated 2PACz films. However, these 2PACz molecules were not observed to fully diffuse to the top surface of perovskite layer (Figure S32b, inset, Supporting Information), as also 2PACz was not detected by XPS (P 2*p*). Therefore, the increased efficiency of small area devices with spray-coated 2PACz may associate with the excess of 2PACz remaining in the perovskite layer, as phosphonic acids have been shown to passivate Pb^{2+} defects.[60]

We showed that the 2PACz can be deposited using spray-coating method and its deposition can be optimized through the WF tuning, resulting in higher PCE. To prove that the WF tuning is an important parameter for the device performance optimization, we employed a wide bandgap triple cation perovskite (1.68 eV). The perovskite composition was changed to $Cs_{0.05}(FA_{0.77}MA_{0.23})_{0.95}Pb(I_{0.77}Br_{0.23})_3$, while the device architecture was maintained unchanged (glass/ITO/2PACz/-perovskite/PEAI/PCBM/BCP/Ag). We then spray-coated 2PACz using different cycles, for optimizing the thickness. As shown in Figure S33a, Supporting Information, the optimum condition for the wide bandgap perovskite is between 5 and 10 cycles, differently to the 10 cycles observed for the low bandgap perovskite devices. This difference shows that the lower WF is more suitable for this perovskite bandgap (Figure S33b, Supporting Information).

The stability of these 2PACz layers was investigated using mass spectroscopy (MS) with the aim to probe their overall stability in devices. We performed MS measurements on ITO/2PACz using spin-coating, evaporation, and spray-coating methods (Figure S34, Supporting Information). The mass-to-charge (m/z) signal of 335 amu, corresponding to the molecular weight of 2PACz, and/or its fragments were not detected during the 1 h light illumination under 1-sun, which raises the sample temperature up to ~60 °C. The above results infer that 2PACz molecules can maintain the strong bonds with ITO under the condition of 1 sun illumination in vacuum conditions (~4.2 × 10^{-6} Pa), regardless of the deposition method. However, it is emphasized that when 2PACz molecules are submitted under a higher temperature of ~220 °C–230 °C (Figure S11, Supporting Information) in N_2 environment, decomposition takes place. Therefore, care should be taken when considering the deposition of 2PACz by the evaporation method. As discussed in the Note S2, Supporting Information (Figure S24 and Table S4, Supporting Information), variations in the full-width at half-maximum (FWHM) values in the XPS N 1*s* core-level region is noticeable when comparing the 50 nm evaporated 2PACz followed by the postdeposition treatment with the spin-coated and spray-coated 2PACz. These results are also in agreement with the ATR results (Figure S11d,e, Supporting Information), where the changes in C–

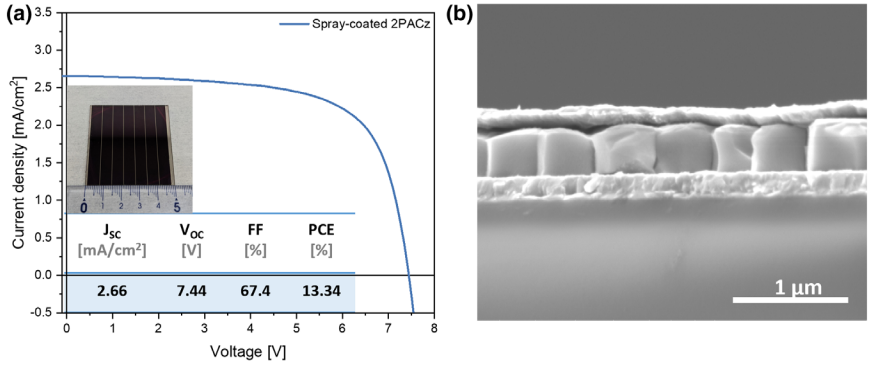

Figure 5. a) Proof-of-concept *J-V* curves of 5 × 5 cm^2 solar modules obtained by depositing 2PACz with spray-coating. The inset shows the picture of a solar module and a table with the *J-V* parameters. b) SEM cross section of the solar module.

N/C–H/C–C bonds were probed comparing the fresh and the remained 2PACz powder in the evaporation crucible.

2.5. Perovskite Solar Modules

We fabricated modules using 5 × 5 cm^2 glass/ITO patterned substrates, consisting of seven sub-cells with an overall aperture area of 22.4 cm^2. The uniformity of 2PACz films deposited on 5 × 5 cm^2 ITO/glass substrates by the three deposition methods of spin-coated, evaporated, and spray-coated techniques were evaluated by AFM and UV–Vis and show similar results (Figures S35–S38, Table S5 and Note S3, Supporting Information). The device architecture was modified slightly to that of small area devices, being glass/ITO/2PACz/perovskite/PEAI/PCBM/C_{60}/SnO_2/Ag, similar to that shown in our previous work.[61] Initially, the triple cation perovskite (1.57 eV bandgap) was used for the fabrication of perovskite solar modules. However, using the one-step spin-coating technique with antisolvent treatment showed low reproducibility issues and low device performance due to the presence of numerous pinholes (Figure S39, Supporting Information). We therefore used a 2-step perovskite deposition method resulting in a similar bandgap (1.56 eV), which has already been shown to be suitable for the fabrication of 5 × 5 cm^2 perovskite solar modules as it does not require antisolvent treatment. This perovskite ($C_{0.05}(FA_{0.5}MA_{0.5})_{0.95}Pb(I_{0.98}Br_{0.02})_3$) produces films with a low density of pinholes[62] (Figure S40, Supporting Information) and high uniformity, as shown by the consistent XRD patterns across all samples and positions (Figure S41, Note S3, Supporting Information). Because the bandgap is very similar to that of the triple cation used for small area devices, we used the same optimal conditions for the 2PACz deposition, that is, 10 cycles for spray-coating and 50 nm thickness with postdeposition treatment for the evaporation. As ETL, in addition to the spin-coated PCBM/BCP, a scaling-up-compatible ETL stack consisting of evaporated C_{60}/BCP is employed on the solar modules. Figure S42, Supporting Information, shows the statistical results obtained on all the perovskite solar modules (5 × 5 cm^2) fabricated in this work using spin-coated 2PACz as HTL. The best perovskite solar module consisting of ($C_{0.05}(FA_{0.5}MA_{0.5})_{0.95}Pb(I_{0.98}Br_{0.02})_3$) perovskite by the 2-step method with the evaporated C_{60}/BCP ETL stack showed higher reproducibility and device performance (PCE of 11.15 ± 1.62%). In the case of the perovskites by the 1-step method followed by the spin-coated PCBM/BCP or evaporated C_{60}/BCP, PCEs of 9.24 ± 2.47% and 9.72 ± 1.50% were achieved, respectively. In particular, for the 1-step and C_{60}/BCP ETL case, only 40% of devices were operational (the others showed shunting behaviors due to the presence of multiple pinholes). Using the optimized conditions for module fabrication, we fabricated a proof-of-concept module obtained with 2PACz deposited by spray-coating. **Figure 5a** shows the *J-V* curve of the module with the highest aperture efficiency of 13.34% (efficiency calculated over the entire illumination region, including the active area and the inactive interconnections).

Comparing the module efficiency to that of a module prepared intentionally without 2PACz HTL (Figure S43, Supporting Information) shows that, without HTL, the module PCE remains considerably lower (below 5%). In Figure 5b, the SEM cross section of a module shows large and ordered perovskite grains with sizes of about >500 nm wide and 450 nm thick. Figure S44, Supporting Information, shows a summary of reported PCEs for perovskite solar modules with different active area sizes using SAMs as HTL.[32,61,63–68] Based on our survey,[69] despite the large success of SAMs in the literature for fabricating small area p-i-n perovskite solar cells, the results of perovskite solar modules made on SAM HTLs underline the inherent decrease in PCE as a function of module size.[70] Furthermore, the highest PCEs in inverted perovskite solar modules in the literature are obtained using one or more traditional HTLs (e.g., PTAA, NiOx)[71–73] or SAMs coupled with these (e.g., PTAA+MeO-2PACz, NiOx+2PACz, NiOx+Me-4PACz, and so on).[73–75] This leads to our understanding that further molecular engineering design is required for boosting the performance of SAM-based large area perovskite solar modules.[69] For example, Sun et al.[76] demonstrated that Al_2O_3 nanoparticles combined with diethyl (4-(3,6-diphenyl-9H-carbazol-9-yl) butyl) phosphonic acid (Ph-4PACz), molecule presenting a large dipole moment (2.32 D), helps boosting the FF when applied in large area devices (e.g., 1 cm^2) leading to a certified PCE of 24.48%. Our systematic investigations of 2PACz deposition by upscalable techniques can be further extended to those new types of SAM HTLs, where further improvements of perovskite solar module efficiencies and stability are expected.

2.6. Conclusion

We have utilized thermal evaporation and spray-coating as alternative techniques to deposit 2PACz HTL in perovskite solar cells and modules. It is in fact very urgent to find methods for the deposition of 2PACz on large area solar modules. For devices employing perovskites with a bandgap of 1.57 eV, the optimized conditions are 50 nm evaporated 2PACz followed by a postdeposition treatment (based on ethanol washing), and 10 cycles of spray-coating. The optimized spin-coating, evaporated, and spray-coated 2PACz-based PSCs achieved average PCEs of 19.7%, 19.3%, and 20.0%, respectively. As proof-of-concept, we have used the optimized spray-coating technique of 2PACz for the fabrication of large area perovskite solar modules with an aperture area of 22.4 cm^2 achieving a PCE of 13.34%. As for the operational stability, we consistently obtained stable power outputs for PSCs with

solution-based methods of spin-coated and spray-coated 2PACz, while the devices with evaporated 2PACz showed poor stability. ATR and XPS analyses performed on the 2PACz before and after the thermal evaporation showed differences in the chemical composition (C–N/C–H/C–C bonds), suggesting that degradation of the 2PACz occurred under high temperature and vacuum conditions, thus affecting the performance and stability of the PSCs. Nevertheless, the degradation can be mitigated by controlling the evaporation temperature (below 200 °C) and reducing the evaporation rate. Combining this work with that of Cassella et al.[23] and Farag et al.,[21] both spray-coating and thermal evaporation techniques find broad applicability for all types of SAMs, although for thermal evaporation, special care should be taken regarding the degradation temperature of each SAM.

Furthermore, using thermal evaporation and spray-coating techniques have shown advantages in analyzing the electronic properties of 2PACz layers, particularly regarding their thickness and morphology. In the case of optimized spray-coated 2PACz, the films are not uniform in morphology showing rough surfaces with a thickness of 7–9 nm. However, the excessive 2PACz is not covalently bond to ITO, and thus, this mixes with the perovskite precursor solution during spin-coating and remains in the perovskite film. In fact, SIMS analysis reveals that the PO_2^- signal (originating from 2PACz) appears in spray-coated 2PACz/-perovskite sample and may correlate with the device performance improvements of spray-coated devices as compared to control (spin-coated 2PACz) devices, due to the SAM passivation effect. KPFM and UPS analyses show the correlation between ITO/2PACz WF and the corresponding device V_{OC}, where higher WF is associated with the increase in average V_{OC} employing thicker 2PACz layers. Thus, thick 2PACz layers help to attain a conformal coverage on the ITO substrate, and the excess of 2PACz remaining in the perovskite layer helps to increase the device performance. Thus, despite it is assured that 2PACz forms a monolayer HTL, its optimum deposition thickness leading to the highest device performances does not necessarily correspond to monolayer characteristics. Currently, numerous new SAM molecules have been reported leading to higher PCEs than 2PACz. Nevertheless, our studies can be further extended to new types of SAM HTLs, where higher efficiencies and stabilities are expected.

3. Experimental Section

Device fabrication: Small area devices were fabricated on substrates 1.5 × 1.5 cm^2, each with four contacts with an active area of 0.16 cm^2. The ITO substrates were cleaned with DI water and detergent, DI water, acetone, and IPA in an ultrasonic bath for 15 min each. The substrate was treated using UV-O_3 cleaner for 15 min immediately before the 2PACz deposition, which was carried out by spin-coating, spray-coating, and thermal evaporation. 2PACz was purchased from TCI. For the solution-processed deposition methods (spin-coating and spray-coating), 2PACz solution (1 mg mL^{-1}) in ethanol was prepared 1 day before the deposition, kept in the glovebox without stirring, and then sonicated for 5 min before use. For the spin-coating process, the 2PACz solution was spin-coated at 3000 rpm for 15 s and then annealed at 100 °C for 5 min. For the spray-coating method, the 2PACz solution was sprayed with an airbrush (Anest Iwata Corp., HP plus nozzle tip diameter φ 0.3 mm) at an angle of 45° and at a distance of 15 cm from the substrates, on a hotplate at 100 °C. After spray-coating, the samples were annealed for an additional 5 min at 100 °C to remove the ethanol in excess. As for the evaporated 2PACz, samples were inserted in a vacuum chamber, a vacuum of ~2–3 × 10^{-4} Pa was reached and then the evaporation was started, using a rate of 0.22 Å s^{-1} measured using a quartz crystal microbalance (QCM). Prior to each deposition, crucibles were cleaned with ethanol, and new powder was used for each evaporation. After evaporation, a post-deposition treatment was performed: Films were annealed at 100 °C for 5 min, then a washing treatment with ethanol was performed to remove the excess 2PACz (spin-coated at 3000 rpm for 15 s), and finally, a second annealing for 5 min at 100 °C was carried out to evaporate the solvent.

Perovskite deposition: In this work, three types of perovskite composition were fabricated.

1 One-step 1.57 eV triple cation ($Cs_{0.05}(FA_{0.83}MA_{0.17})_{0.95}Pb(I_{0.95}Br_{0.05})_3$), for small area devices with narrow bandgap. The precursor solution was prepared by dissolving cesium iodide (CsI, Aldrich), methylammonium bromine (MABr, Dyenamo), formamidinium iodide (FAI, Dyenamo), and lead iodide (PbI_2, TCI) in 4:1 N,N-dimethylformamide (DMF, Fujifilm Wako) to dimethyl sulfoxide (DMSO, Fujifilm Wako). The solution was heated up for 60 min at 65 °C and left to cool down, then filtered in a glove box using a 0.22 μm filter (PVDF, Millex-GV). The precursor was then spin-coated in a nitrogen glovebox at 3000 rpm for 40 s, where ethyl acetate (EA, Fujifilm) antisolvent was dripped statically at 20 s. The film was subsequently annealed at 100 °C for 20 min.
2 One-step 1.68 eV triple cation, for small area devices with wide bandgap. The precursor solution was prepared using the same chemicals as above but with different composition ($Cs_{0.05}(FA_{0.77}MA_{0.23})_{0.95}Pb(I_{0.77}Br_{0.23})_3$). The solution was heated up for 60 min at 60 °C and left to cool down, and then filtered in a glove box using a 0.22 μm filter (PVDF, Millex-GV). The precursor was spin-coated in a nitrogen glovebox at 5000 rpm for 90 s, using EA as antisolvent, which was dripped statically at 40 s, and then the film was annealed at 100 °C for 30 min.
3 Two-step 1.57 eV perovskite ($C_{0.05}(FA_{0.5}MA_{0.5})_{0.95}Pb(I_{0.98}Br_{0.02})_3$), for module fabrication with narrow bandgap. A solution of 1.35 M PbI_2 and 0.0675 M CsI was dissolved in DMF/DMSO (19:1) and was spin-coated at 3000 rpm for 30 s and annealed for 1 min at 70 °C. The organic precursor solution was prepared using FAI (40 mg), MAI (20 mg), MABr (7.5 mg), and MACl (5 mg) in isopropyl alcohol (1 mL, IPA, Fujifilm Wako) and was then spin-coated onto the PbI_2/CsI layer at 3000 rpm for 30 s and annealed at 70 °C for 1 min and then 150 °C for 10 min. Both depositions were performed in a dry room, with temperature of ~18 °C and a relative humidity (RH) of 15%–20%.

2-phenethylamine hydroiodide (PEAI, TCI) was dissolved in IPA (1.25 mg mL^{-1}, IPA, Fujifilm Wako). The solution was spin-coated at 5000 rpm for 30 s and further annealed at 100 °C for 10 min.

Phenyl-C61-butyric acid methyl ester (PCBM, TCI) solution (20 mg mL^{-1}) in 1,2-Dichlorobenzene (Thermo Scientific), was prepared 24 h before use under stirring and then filtered using a 0.22 μm filter (PVDF, Millex-GV). The solution was spin-coated at 1000 rpm for 45 s and then annealed for 10 min at 70 °C.

Bathocuproine (BCP, TCI) solution was also prepared 24 h ahead under stirring, by dissolving BCP (2 mg) in IPA (1 mL), then filtered and spin-coated at 6000 rpm for 30 s, and then annealed for 5 min. Seventy nanometers of silver (Ag), were thermally evaporated under a vacuum of around 10^{-5} Torr, the first 10 nm was evaporated at a low rate (~0.2 Å s^{-1}), and then the evaporation rate was gradually increased up to 1.5 Å s^{-1}.

Module fabrication: For module fabrication, 5 × 5 cm^2 glass/ITO patterned (P1) was used and 2PACz was deposited using spin-coating and spray-coating. Then, the perovskite layer by a 2-step method was deposited using spin-coating inside a dry room, and PEAI surface treatment was used in the same way as for small area solar cells (dynamic spin-coating using tilted angle to cover the full device surface, 5000 rpm for 30 s, and then annealed at 100 °C for 10 min). A PCBM solution (5 mg·mL^{-1}) in chlorobenzene (Fujifilm) was spin-coated at 2000 rpm for 45 s. The modules were transferred in an evaporator chamber for the deposition of C_{60} (18 nm, TCI) and BCP (8 nm, TCI). For our best device with spray-coated 2PACz presented in Figure 5a, BCP was replaced with SnO_2 (20 nm) deposited by ALD (tetrakis(dimethylamino)tin(IV) (TDMASn) precursor; ALD, Cambridge Nanotechnology, Savannah S200). Then, P2 laser scribing was performed, and 80 nm of Ag were deposited as back contact on the whole device surface (no mask) using thermal evaporation. Finally, the P3 laser scribing was performed before the PCE measurement. The total area of perovskite solar modules is 25 cm^2 and the aperture area is 22.4 cm^2.

Characterization methods: J-V and MPP were measured using Keithley 2400 source meter and a solar simulator (Oriel, Sol1A, Newport) with a

calibrated AM1.5 lamp (100 mW cm^{-2}). The *J-V* measurements and MPPT were performed in a dry room with relative humidity of ~20% and temperature <20 °C. For the MPPT, all parameters were analyzed over time. The first point in the MPPT was used for normalization. As for the long-term steady-state operational stability measurements, the devices were loaded in the home-designed enclosure box and a nitrogen gas flow was kept constant for all samples to ensure similar temperature conditions between all samples (~29–30 °C). The solar simulator lamp was calibrated each time before starting the measurement to ensure accurate light intensity. Keithley 2401 source meter controlled by a customized LabVIEW program was used to apply a fixed voltage (V_{MPP}). Samples were measured two times for both spin- and spray-coated 2PACz, using different batch conditions to make sure that the data were reproducible. However, in the case of devices prepared using evaporated 2PACz, the measurements have been repeated three times, due to their different behaviors.

ATR was performed on 2PACz fresh and aged powders using a Fourier Transform Infrared Spectrometer (Bruker, Vertex 80 V).

The steady-state PL spectra were taken using a JASCO FP-8500 spectrophotometer, using excitation wavelength of 790 nm.

The UV–Vis spectra were recorded using a JASCO V-670 spectrophotometer.

SEM images were taken using a FEI Quanta 250 scanning electron microscope.

Contact angle measurements were conducted using a drop shape analyzer (FM 4000, Krüss GmbH, Germany).

Tapping mode AFM images were acquired using ASYLUM-MFP-3D equipment with standard silicon cantilevers and a nominal spring constant of 48 Nm^{-1} and a resonant frequency of 190 kHz (AFM cantilever model number and manufacturer: Tap 190Al-G from Budget Sensors).

The chemical compositions and energy levels were determined by XPS and UPS, respectively, on a photoelectron spectrometer (XPS-AXIS Ultra HAS, Kratos) equipped with monochromatic Al-Ka = 1486.6 eV and nonmonochromatic He–Iα = 21.22 eV sources with a probing area of 300 × 700 μm^2. The binding energy scales for UPS and XPS were calibrated by measuring the Fermi edge (E_F = 0 eV) and Au $4f_{7/2}$ (84.0 eV) on a clean Au surface. For all the 2PACz/ITO samples, the In 3*d* peaks were compared and observed to be all aligned, indicating minimum or no sample charging phenomena in our XPS measurements.

Low-energy inverse photoemission spectroscopy (LEIPS, ALS Technology Co., Ltd) measurements were performed in an ultrahigh vacuum chamber with a pressure of ~10^{-10} Torr.

Acknowledgements

S.M. and I.N.R. contributed equally to this work. This work was supported by funding from the Energy Materials and Surface Sciences Unit of the Okinawa Institute of Science and Technology Graduate University, the OIST R&D Cluster Research Program, the OIST Proof of Concept (POC) Program, the JSPS KAKENHI Grant Number JP21F21754 and Alexander von Humboldt Foundation. We thank the OIST Micro/Nanofabrication Section and Imaging Section for the support. Biorender software was used for generating Figure 1a.

Conflict of Interest

The authors declare no conflict of interest.

Data Availability Statement

The data that support the findings of this study are available from the corresponding author upon reasonable request.

Supporting Information

Supporting Information is available from the Wiley Online Library or from the author.

Keywords

2PACz, Evaporation, Perovskite solar cells, Self-assembled monolayer, Spray-coating

Received: May 18, 2024
Revised: July 11, 2024
Published online: July 17, 2024

[1] K. P. Bhandari, R. J. Ellingson, A Comprehensive Guide to Solar Energy Systems: With Special Focus on Photovoltaic Systems. (Eds: T. M. Letcher and V. M. Fthenakis), Academic Press, United Kingdom **2018**, Ch. 11.
[2] J. Fan, B. Jia, M. Gu, *Photon. Res.* **2014**, *2*, 111.
[3] Z. Wu, E. Bi, L. K. Ono, D. Li, O. M. Bakr, Y. Yan, Y. B. Qi, *Nano Energy* **2023**, *115*, 108731.
[4] N. Kwon, J. Lee, M. J. Ko, Y. Y. Kim, J. Seo, *Nano Converg.* **2023**, *10*, 28.
[5] Best Research-Cell Efficiency Chart | Photovoltaic Research | NREL.
[6] J. Park, J. Kim, H.-S. Yun, M. J. Paik, E. Noh, H. J. Mun, M. G. Kim, J. Shin, S. Il Seok, *Nature* **2023**, *616*, 724.
[7] B. Li, W. Zhang, *Commun. Mater.* **2022**, *3*, 65.
[8] Y. Cheng, L. Ding, *SusMat* **2021**, *1*, 324.
[9] Y. Yao, C. Cheng, C. Zhang, H. Hu, K. Wang, S. De Wolf, Y. Yao, C. Cheng, C. Zhang, K. Wang, H. Hu, S. De Wolf, *Adv. Mater.* **2022**, *34*, 2203794.
[10] A. Al-Ashouri, A. Magomedov, M. Roß, M. Jošt, M. Talaikis, G. Chistiakova, T. Bertram, J. A. Márquez, E. Köhnen, E. Kasparavičius, S. Levcenco, L. Gil-Escrig, C. J. Hages, R. Schlatmann, B. Rech, T. Malinauskas, T. Unold, C. A. Kaufmann, L. Korte, G. Niaura, V. Getautis, S. Albrecht, *Energ. Environ. Sci.* **2019**, *12*, 3356.
[11] A. Al-Ashouri, E. Köhnen, B. Li, A. Magomedov, H. Hempel, P. Caprioglio, J. A. Márquez, A. B. M. Vilches, E. Kasparavicius, J. A. Smith, N. Phung, D. Menzel, M. Grischek, L. Kegelmann, D. Skroblin, C. Gollwitzer, T. Malinauskas, M. Jošt, G. Matič, B. Rech, R. Schlatmann, M. Topič, L. Korte, A. Abate, B. Stannowski, D. Neher, M. Stolterfoht, T. Unold, V. Getautis, S. Albrecht, *Science* **2020**, *370*, 1300.
[12] S. A. Paniagua, E. L. Li, S. R. Marder, *Phys. Chem. Chem. Phys.* **2014**, *16*, 2874.
[13] S. Mariotti, E. Köhnen, F. Scheler, K. Sveinbjörnsson, L. Zimmermann, M. Piot, F. Yang, B. Li, J. Warby, A. Musiienko, D. Menzel, F. Lang, S. Keßler, I. Levine, D. Mantione, A. Al-Ashouri, M. S. Härtel, K. Xu, A. Cruz, J. Kurpiers, P. Wagner, H. Köbler, J. Li, A. Magomedov, D. Mecerreyes, E. Unger, A. Abate, M. Stolterfoht, B. Stannowski, R. Schlatmann, L. Korte, S. Albrecht, *Science (1979)* **2023**, *381*, 63.
[14] I. Levine, A. Al-Ashouri, A. Musiienko, T. Unold, S. Albrecht, T. Dittrich, *Joule* **2021**, *5*, 2915.
[15] C. Zhang, S. Mariotti, L. K. Ono, C. Ding, K. Mitrofanov, C. Zhang, S. Yuan, P. Ji, J. Zhang, T. Wu, R. Kabe, Y. B. Qi, *J. Mater. Chem. C* **2023**, *11*, 2851.
[16] E. Erdenebileg, N. Tiwari, F. U. Kosasih, H. A. Dewi, L. Jia, N. Mathews, S. Mhaisalkar, A. Bruno, *Mater. Today Chem.* **2023**, *30*, 101575.
[17] N. Phung, M. Verheijen, A. Todinova, K. Datta, M. Verhage, A. Al-Ashouri, H. Köbler, X. Li, A. Abate, S. Albrecht, M. Creatore, *ACS Appl. Mater. Interfaces* **2022**, *14*, 2166.
[18] G. Tong, J. Zhang, T. Bu, L. K. Ono, C. Zhang, Y. Liu, C. Ding, T. Wu, S. Mariotti, S. Kazaoui, Y. B. Qi, *Adv. Energy Mater.* **2023**, *13*, 2300153.
[19] F. Jafarzadeh, L. A. Castriotta, F. De Rossi, J. Ali, F. Di Giacomo, A. Di Carlo, F. Matteocci, F. Brunetti, *Sustain. Energy Fuels* **2023**, *7*, 2219.
[20] M. Härtel, B. Li, S. Mariotti, P. Wagner, F. Ruske, S. Albrecht, B. Szyszka, *Sol. Energy Mater. Sol. Cells* **2023**, *252*, 112180.
[21] A. Farag, T. Feeney, I. M. Hossain, F. Schackmar, P. Fassl, K. Küster, R. Bäuerle, M. A. Ruiz-Preciado, M. Hentschel, D. B. Ritzer, A. Diercks, Y.

Li, B. A. Nejand, F. Laufer, R. Singh, U. Starke, U. W. Paetzold, *Adv. Energy Mater.* **2023**, *13*, 2203982.
[22] A. Harter, S. Mariotti, L. Korte, R. Schlatmann, S. Albrecht, B. Stannowski, *Prog. Photovolt. Res. Appl.* **2023**, *31*, 813.
[23] E. J. Cassella, E. L. K. Spooner, T. Thornber, M. E. O'Kane, T. E. Catley, J. E. Bishop, J. A. Smith, O. S. Game, D. G. Lidzey, *Adv. Sci.* **2022**, *9*, 2104848.
[24] C. Girotto, B. P. Rand, J. Genoe, P. Heremans, *Sol. Energy Mater. Sol. Cells* **2009**, *93*, 454.
[25] A. Al-Ashouri, M. Marčinskas, E. Kasparavičius, T. Malinauskas, A. Palmstrom, V. Getautis, S. Albrecht, M. D. McGehee, A. Magomedov, *ACS Energy Lett.* **2023**, *8*, 898.
[26] J. Walton, M. R. Alexander, N. Fairley, P. Roach, A. G. Shard, *Surf. Interface Anal.* **2016**, *48*, 164.
[27] X. Zheng, Z. Li, Y. Zhang, M. Chen, T. Liu, C. Xiao, D. Gao, J. B. Patel, D. Kuciauskas, A. Magomedov, R. A. Scheidt, X. Wang, S. P. Harvey, Z. Dai, C. Zhang, D. Morales, H. Pruett, B. M. Wieliczka, A. R. Kirmani, N. P. Padture, K. R. Graham, Y. Yan, M. K. Nazeeruddin, M. D. McGehee, Z. Zhu, J. M. Luther, *Nat. Energy* **2023**, *8*, 462.
[28] D. H. Kim, S. Lee, G. M. Kim, S. Y. Oh, *Electron. Mater. Lett.* **2023**, *19*, 510.
[29] Z. Zhu, K. Mao, K. Zhang, W. Peng, J. Zhang, H. Meng, S. Cheng, T. Li, H. Lin, Q. Chen, X. Wu, J. Xu, *Joule* **2022**, *6*, 2849.
[30] Z. Li, X. Sun, X. Zheng, B. Li, D. Gao, S. Zhang, X. Wu, S. Li, J. Gong, J. M. Luther, Z. Li, Z. Zhu, *Science (1979)* **2023**, *382*, 284.
[31] S. Zhang, F. Ye, X. Wang, R. Chen, H. Zhang, L. Zhan, X. Jiang, Y. Li, X. Ji, S. Liu, M. Yu, F. Yu, Y. Zhang, R. Wu, Z. Liu, Z. Ning, D. Neher, L. Han, Y. Lin, H. Tian, W. Chen, M. Stolterfoht, L. Zhang, W. H. Zhu, Y. Wu, *Science (1979)* **2023**, *380*, 404.
[32] S. M. Park, M. Wei, J. Xu, H. R. Atapattu, F. T. Eickemeyer, K. Darabi, L. Grater, Y. Yang, C. Liu, S. Teale, B. Chen, H. Chen, T. Wang, L. Zeng, A. Maxwell, Z. Wang, K. R. Rao, Z. Cai, S. M. Zakeeruddin, J. T. Pham, C. M. Risko, A. Amassian, M. G. Kanatzidis, K. R. Graham, M. Grätzel, E. H. Sargent, *Science (1979)* **2023**, *381*, 209.
[33] R. Azmi, E. Ugur, A. Seitkhan, F. Aljamaan, A. S. Subbiah, J. Liu, G. T. Harrison, M. I. Nugraha, M. K. Eswaran, M. Babics, Y. Chen, F. Xu, T. G. Allen, A. ur Rehman, C. L. Wang, T. D. Anthopoulos, U. Schwingenschlögl, M. De Bastiani, E. Aydin, S. De Wolf, *Science (1979)* **2022**, *376*, 73.
[34] W. Peng, K. Mao, F. Cai, H. Meng, Z. Zhu, T. Li, S. Yuan, Z. Xu, X. Feng, J. Xu, M. D. McGehee, J. Xu, *Science (1979)* **2023**, *379*, 683.
[35] G. Li, Z. Su, L. Canil, D. Hughes, M. H. Aldamasy, J. Dagar, S. Trofimov, L. Wang, W. Zuo, J. J. Jerónimo-Rendon, M. M. Byranvand, C. Wang, R. Zhu, Z. Zhang, F. Yang, G. Nasti, B. Naydenov, W. C. Tsoi, Z. Li, X. Gao, Z. Wang, Y. Jia, E. Unger, M. Saliba, M. Li, A. Abate, *Science (1979)* **2023**, *379*, 399.
[36] Q. Tan, Z. Li, G. Luo, X. Zhang, B. Che, G. Chen, H. Gao, D. He, G. Ma, J. Wang, J. Xiu, H. Yi, T. Chen, Z. He, *Nature* **2023**, *620*, 545.
[37] F. Li, X. Deng, Z. Shi, S. Wu, Z. Zeng, D. Wang, Y. Li, F. Qi, Z. Zhang, Z. Yang, S. H. Jang, F. R. Lin, S.-W. Tsang, X. K. Chen, A. K. Y. Jen, *Nat. Photon.* **2023**, *17*, 478.
[38] H. Chen, S. Teale, B. Chen, Y. Hou, L. Grater, T. Zhu, K. Bertens, S. M. Park, H. R. Atapattu, Y. Gao, M. Wei, A. K. Johnston, Q. Zhou, K. Xu, D. Yu, C. Han, T. Cui, E. H. Jung, C. Zhou, W. Zhou, A. H. Proppe, S. Hoogland, F. Laquai, T. Filleter, K. R. Graham, Z. Ning, E. H. Sargent, *Nat. Photon.* **2022**, *16*, 352.
[39] Q. An, F. Paulus, D. Becker-Koch, C. Cho, Q. Sun, A. Weu, S. Bitton, N. Tessler, Y. Vaynzof, *Matter* **2021**, *4*, 1683.
[40] M. Li, J. Zhou, L. Tan, H. Li, Y. Liu, C. Jiang, Y. Ye, L. Ding, W. Tress, C. Yi, *Innov.* **2022**, *3*, 100310.
[41] H. Wang, F. Yang, N. Li, M. A. Kamarudin, J. Qu, J. Song, S. Hayase, C. J. Brabec, *ACS Sustain. Chem. Eng.* **2020**, *8*, 8848.
[42] W. Chen, H. Sun, Q. Hu, A. B. Djurišić, T. P. Russell, X. Guo, Z. He, *ACS Energy Lett.* **2019**, *4*, 2535.
[43] H. Oh, G. Kang, M. Park, *ACS Appl. Energy Mater.* **2022**, *5*, 15844.
[44] T. Lemercier, L. Perrin, S. Berson, L. Flandin, E. Planes, *Mater. Adv.* **2021**, *2*, 7907.
[45] 2PACz 20999–38-6 | Tokyo Chemical Industry Co., Ltd.(JP).
[46] L. Zuo, Z. Gu, T. Ye, W. Fu, G. Wu, H. Li, H. Chen, *J. Am. Chem. Soc.* **2015**, *137*, 2674.
[47] S. Bai, P. Da, C. Li, Z. Wang, Z. Yuan, F. Fu, M. Kawecki, X. Liu, N. Sakai, J. T. W. Wang, S. Huettner, S. Buecheler, M. Fahlman, F. Gao, H. J. Snaith, *Nature* **2019**, *571*, 245.
[48] L. Canil, T. Cramer, B. Fraboni, D. Ricciarelli, D. Meggiolaro, A. Singh, M. Liu, M. Rusu, C. M. Wolff, N. Phung, Q. Wang, D. Neher, T. Unold, P. Vivo, A. Gagliardi, F. De Angelis, A. Abate, *Energ. Environ. Sci.* **2021**, *14*, 1429.
[49] Y. Yang, S. Cheng, X. Zhu, S. Li, Z. Zheng, K. Zhao, L. Ji, R. Li, Y. Liu, C. Liu, Q. Lin, N. Yan, Z. Wang, *Nat. Energy* **2023**, *8*, 978.
[50] L. Chen, Q. Chen, C. Wang, Y. Li, *J. Am. Chem. Soc.* **2020**, *142*, 18281.
[51] H. Hoppe, T. Glatzel, M. Niggemann, A. Hinsch, M. C. Lux-Steiner, N. S. Sariciftci, *Nano Lett.* **2005**, *5*, 269.
[52] N. Fairley, V. Fernandez, M. Richard-Plouet, C. Guillot-Deudon, J. Walton, E. Smith, D. Flahaut, M. Greiner, M. Biesinger, S. Tougaard, D. Morgan, J. Baltrusaitis, *Appl. Surf. Sci. Adv.* **2021**, *5*, 100112.
[53] E. Hoque, J. A. DeRose, B. Bhushan, K. W. Hipps, *Ultramicroscopy* **2009**, *109*, 1015.
[54] C. R. Brundle, B. V. Crist, P. S. Bagus, *J. Vac. Sci. Technol. A* **2021**, *39*, 63206.
[55] NIST Standard Reference Database 71 | NIST.
[56] S. Tanuma, C. J. Powell, D. R. Penn, *Surf. Interface Anal.* **1994**, *21*, 165.
[57] A. Laforgue, T. Addou, D. Bélanger, *Langmuir* **2005**, *21*, 6855.
[58] E. J. Juarez-Perez, Z. Hawash, S. R. Raga, L. K. Ono, Y. B. Qi, *Energ. Environ. Sci.* **2016**, *9*, 3406.
[59] E. J. Juarez-Perez, L. K. Ono, M. Maeda, Y. Jiang, Z. Hawash, Y. B. Qi, *J. Mater. Chem. A Mater.* **2018**, *6*, 9604.
[60] M. Gao, X. Xu, H. Tian, P. Ran, Z. Jia, Y. Su, J. Hui, X. Gan, S. Zhao, H. Zhu, H. Lv, Y. "Michael" Yang, *J. Phys. Chem. Lett.* **2024**, *15*, 4015.
[61] T. Wu, X. Xu, L. K. Ono, T. Guo, S. Mariotti, C. Ding, S. Yuan, C. Zhang, J. Zhang, K. Mitrofanov, Q. Zhang, S. Raj, X. Liu, H. Segawa, P. Ji, T. Li, R. Kabe, L. Han, A. Narita, Y. B. Qi, *Adv. Mater.* **2023**, *35*, 2300169.
[62] T. Bu, L. K. Ono, J. Li, J. Su, G. Tong, W. Zhang, Y. Liu, J. Zhang, J. Chang, S. Kazaoui, F. Huang, Y. B. Cheng, Y. B. Qi, *Nat. Energy* **2022**, *7*, 528.
[63] B. Abdollahi Nejand, D. B. Ritzer, H. Hu, F. Schackmar, S. Moghadamzadeh, T. Feeney, R. Singh, F. Laufer, R. Schmager, R. Azmi, M. Kaiser, T. Abzieher, S. Gharibzadeh, E. Ahlswede, U. Lemmer, B. S. Richards, U. W. Paetzold, *Nat. Energy* **2022**, *7*, 620.
[64] J. Zeng, L. Bi, Y. Cheng, B. Xu, A. K. Y. Jen, *Nano Res. Energy* **2022**, *1*, e9120004.
[65] J. Dagar, M. Fenske, A. Al-Ashouri, C. Schultz, B. Li, H. Köbler, R. Munir, G. Parmasivam, J. Li, I. Levine, A. Merdasa, L. Kegelmann, H. Näsström, J. A. Marquez, T. Unold, D. M. Többens, R. Schlatmann, B. Stegemann, A. Abate, S. Albrecht, E. Unger, *ACS Appl. Mater. Interfaces* **2021**, *13*, 13022.
[66] E. Li, E. Bi, Y. Wu, W. Zhang, L. Li, H. Chen, L. Han, H. Tian, W.-H. Zhu, E. Li, Y. Wu, W. Zhang, L. Li, H. Tian, W. Zhu, E. Bi, H. Chen, L. Han, *Adv. Funct. Mater.* **2020**, *30*, 1909509.
[67] H. Cheng, Y. Li, Y. Zhong, *Mater. Chem. Front.* **2023**, *7*, 3958.
[68] Y. Yang, Y. Wang, Z. Qu, K. Zhang, T. Liang, S. Chen, W. Lv, F. Min, Y. Chen, Y. Qiao, Y. Song, *Angew. Chem.* **2023**, *62*, e202300971.
[69] T. Wu, S. Mariotti, P. Ji, L. K. Ono, T. Guo, I. N. Rabehi, S. Yuan, J. Zhang, C. Ding, Z. Guo, Y. B. Qi, *Adv. Funct. Mater.* **2024**, 2316500.
[70] R. Guo, X. Zhang, X. Zheng, L. Li, M. Li, Y. Zhao, S. Zhang, L. Luo, S. You, W. Li, Z. Gong, R. Huang, Y. Cui, Y. Rong, H. Zeng, X. Li, R. Guo, X. Zhang, X. Zheng, L. Li, M. Li, Y. Zhao, S. Zhang, L. Luo, S. You, W. Li, Y. Rong, H. Zeng, X. Li, Z. Gong, R. Huang, Y. Cui, *Adv. Funct. Mater.* **2023**, *33*, 2211955.

[71] Y. Gao, C. Liu, Y. Xie, R. Guo, X. Zhong, H. Ju, L. Qin, P. Jia, S. Wu, R. E. I. Schropp, Y. Mai, *Adv. Energy Mater.* **2022**, *12*, 2202287.
[72] S. Chen, X. Dai, S. Xu, H. Jiao, L. Zhao, J. Huang, *Science* **2021**, *373*, 902.
[73] S. Liu, V. P. Biju, Y. B. Qi, W. Chen, Z. Liu, *NPG Asia Mater.* **2023**, *15*, 27.
[74] X. Zhang, W. Qiu, S. Apergi, S. Singh, P. Marchezi, W. Song, C. Sternemann, K. Elkhouly, D. Zhang, A. Aguirre, T. Merckx, A. Krishna, Y. Shi, A. Bracesco, C. van Helvoirt, F. Bens, V. Zardetto, J. D'Haen, A. Yu, G. Brocks, T. Aernouts, E. Moons, S. Tao, Y. Zhan, Y. Kuang, J. Poortmans, *ACS Energy Lett.* **2023**, *8*, 2532.
[75] S. Li, X. Wang, H. Li, J. Fang, D. Wang, G. Xie, D. Lin, S. He, L. Qiu, *Small* **2023**, *19*, 2301110.
[76] A. Sun, C. Tian, R. Zhuang, C. Chen, Y. Zheng, X. Wu, C. Tang, Y. Liu, Z. Li, B. Ouyang, J. Du, Z. Li, J. Cai, J. Chen, X. Wu, Y. Hua, C. C. Chen, *Adv. Energy Mater.* **2024**, *14*, 2303941.